NANO · MICRO small
www.small-journal.com

Surface Engineering of Biodegradable Magnesium Alloys for Enhanced Orthopedic Implants

Yixuan Li, Sheng Zhao, Sirong Li, Yuxiang Ge, Rongliang Wang, Liming Zheng, Jiankun Xu, Minghui Sun, Qing Jiang, Yifeng Zhang,* and Hui Wei**

Magnesium (Mg) alloys have been promised for biomedical implants in orthopedic field, however, the fast corrosion rate and mode challenge their clinical application. To push Mg alloys materials into practice, a composite coating with biodegradable and high compatible components to improve anticorrosion property of an Mg alloy (i.e., AZ31) is designed and fabricated. The inner layer is micro-nano structured $Mg(OH)_2$ through hydrothermal treatment. Then stearic acid (SA) is introduced to modify $Mg(OH)_2$ for better reducing the gap below a surface-degradation polymer layer of poly(1,3-trimethylene carbonate). Benefited by the SA modification effect, this sandwiched coating avoids corrosive medium penetration via enhancing the adhesion strength at the interface between outer and inner layers. Both in vitro and in vivo tests indicate that the composite coating modified AZ31 perform a better anticorrosion behavior and biocompatibility compared to bare AZ31. Strikingly, a 1.7-fold improvement in volume of newly formed bone is observed surrounding the composite coating modified implant after 12 week implantation. The sandwiched biocompatible coating strategy paves a hopeful way for future translational application of Mg alloys orthopedic materials in clinics.

1. Introduction

With the elderly population steadily growing, the demand for orthopedic devices is ever increasing.[1] Permanent orthopedics implants based on bioinert metals, such as stainless steel, titanium alloys, and cobalt alloys, have been widely applied for bone stabilization and function recovery.[2,3] However, their mechanical stiffness does not perfectly match natural cortical bones, which can lead to the stress-shielding effect and subsequently the reduction in the surrounding bone density in long-term implantation.[4–6] The permanent orthopedics implants may also need to be removed after healing under certain circumstances.[7] In this regard, developing biodegradable orthopedics implants with proper mechanical properties not only minimizes the stress-shielding effect, but also abrogates the need of secondary-removal surgery and the associated complications.[8]

Among the various materials for biodegradable orthopedics implants, magnesium (Mg) alloys are promising in several aspects.[9] Mg alloys have a Young's modulus (40–45 GPa) close to human natural cortical bone (10–30 GPa).[8,10] Moreover, they degrade in physiological medium during bone healing process.[11–13] Many animal and clinical investigations have established the full biodegradability and good biocompatibility of Mg alloys.[14,15] Nevertheless, their great promise in orthopedics implants has not been fulfilled yet. This is mainly

Y. Li, Y. Ge, R. Wang, L. Zheng, Prof. Q. Jiang, Prof. Y. Zhang
State Key Laboratory of Pharmaceutical Biotechnology
Department of Sports Medicine and Adult Reconstructive Surgery
Nanjing Drum Tower Hospital
The Affiliated Hospital of Nanjing University Medical School
Nanjing 210008, China
E-mail: qingj@nju.edu.cn; zhangyf3@shanghaitech.edu.cn

S. Zhao, S. Li, Prof. H. Wei
College of Engineering and Applied Sciences
Nanjing National Laboratory of Microstructures
Jiangsu Key Laboratory of Artificial Functional Materials
Nanjing University
Nanjing 210093, China
E-mail: weihui@nju.edu.cn

The ORCID identification number(s) for the author(s) of this article can be found under https://doi.org/10.1002/smll.201904486.

DOI: 10.1002/smll.201904486

Dr. J. Xu
Musculoskeletal Research Laboratory
Department of Orthopedics and Traumatology
The Chinese University of Hong Kong
Hong Kong 999077, China

Dr. M. Sun
Department of Joint Surgery
Nanjing Drum Tower Hospital
The Affiliated Hospital of Nanjing University Medical School
Nanjing 210008, China

Prof. Y. Zhang
School of Life Science and Technology
Shanghai Tech University
Shanghai 201210, China

Prof. H. Wei
State Key Laboratory of Analytical Chemistry for Life Science and State Key Laboratory of Coordination Chemistry
School of Chemistry and Chemical Engineering
Nanjing University
Nanjing 210023, China

attributed to their too fast degradation, which not only produces locally high concentration of Mg^{2+} and alkalization to damage the surrounding tissue,[16] but also generates undesirable subcutaneous H_2 gas cavities to retard bone healing.[8] In addition, the localized pitting corrosion leads to uncontrolled degradation of implants, which significantly weakens the mechanical integrity and causes rapid failure of Mg alloys implants during fixation.[13] Therefore, it is urgent to modulate both the degradation rate and mode of Mg alloys implants with the aims to maintain the mechanical integrity and minimize the production of Mg^{2+}, OH^-, and H_2 during the initial stage (especially the first 3 months) after implantation.

Till now, a few surface/interface engineering strategies (e.g., inorganic, metallic, organic, and polymeric coatings) have been developed to improve the anti-corrosion properties of Mg alloys.[17–19] Chemical and electrochemical surface modifications (such as micro arc oxidation and electrodeposition) as well as surface mechanical treatment (such as shot peening and burnishing) are widely applied.[20–23] Among them, polymeric coatings are advantageous over the others because of their biocompatibility, mechanical stability, controllable degradation, and low fabrication cost.[24] Recent studies showed that polymeric coatings (e.g., poly(lactide-co-glycolic) acid (PLGA)) delayed the degradation of Mg alloys.[25] Nevertheless, the bulk erosion of poly(lactic acid) (PLA) or PLGA made the coating easily ruptured and brittle.[26,27] In addition, the incompatibility between a Mg alloy and a polymeric coating weakened the adhesion interaction and generated space between them, allowing physiological medium permeation and leading to subsequent corrosive damage.[24]

To tackle these challenges, herein we developed an innovative surface engineering strategy to enhance Mg alloys implants for bone defect repair by modulating the degradation mode, slowing down the degradation rate, and promoting the new bone regeneration (**Figure 1**). The Mg alloy (AZ31) was coated with a rationally designed coating of magnesium hydroxide ($Mg(OH)_2$), stearic acid (SA), and poly(1,3-trimethylene carbonate) (PTMC). Because of the synergistic effect of coating components, the remarkably enhanced corrosion resistance, cytocompatibility, and new bone regeneration in vivo were achieved.

2. Results and Discussion

2.1. Design Strategy of Polymeric Composite Coating to Enhance Mg Alloy Implants

With the above-mentioned challenges in mind, here we designed and fabricated a composite coating for Mg alloy-based implants as follows (Figure 1).

First, AZ31 and PTMC were chosen as a representative Mg alloy and a polymeric coating, respectively. PTMC degrades in a surface erosion manner, which is different from bulk degradation polymers, such as PLGA, PLA, and polycaprolactone (PCL).[26] Therefore, in comparison with bulk degradation polymers, a PTMC coating would prevent corrosive medium permeation and maintain the mechanical integrity of Mg alloys implants for a longer period.[26,28,29]

Second, to enhance the weak adhesion strength between PTMC and AZ31, their contact area was expanded by in situ forming a micro-nano structured $Mg(OH)_2$ film as an inner layer. The $Mg(OH)_2$ layer was formed by using a facile and environment-friendly hydrothermal approach.[30,31]

Third, SA was used to further alleviate the incompatibility at the interface between $Mg(OH)_2$ layer and PTMC layer. The carboxyl group of SA was covalently anchored onto $Mg(OH)_2$

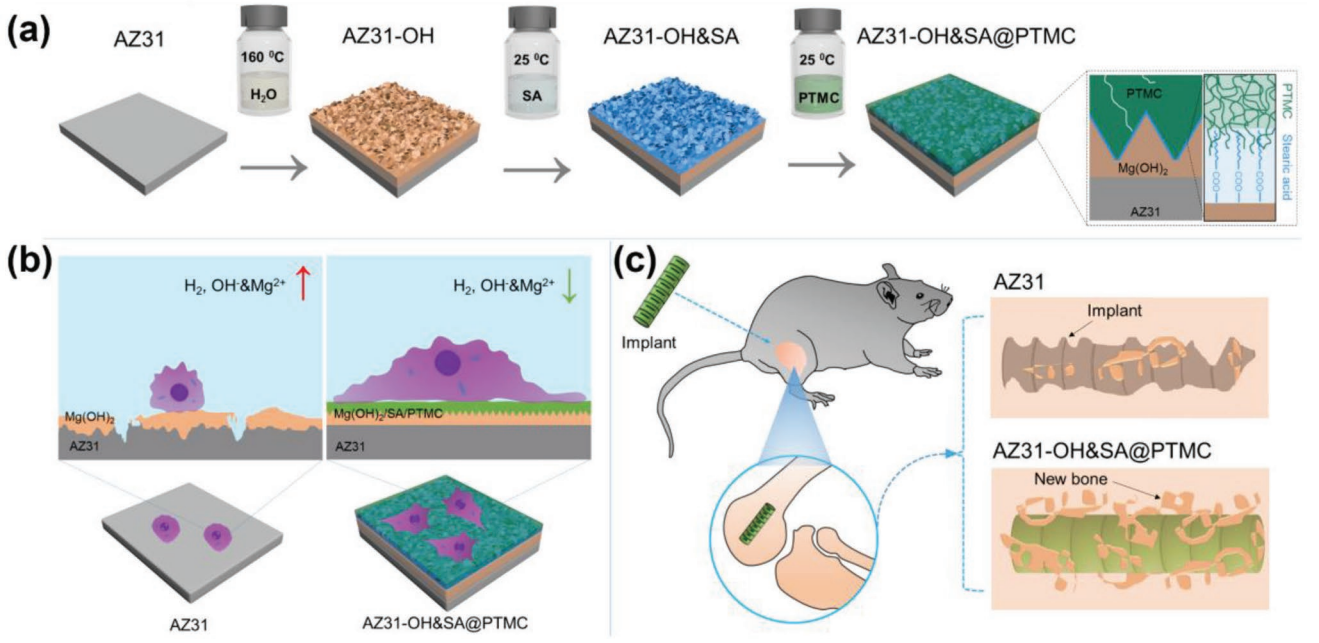

Figure 1. Schematic illustration of Mg alloy orthopedic implant with a sandwiched composite coating. a) Fabrication process of the composite coating on Mg alloy for bone implants. b) Effects on the microenvironment of Mg alloy surface from the sandwiched composite coating in vitro. c) Slowed biodegradation and enhanced bone repair of Mg alloy orthopedic implant with the composite coating in vivo.

to generate magnesium stearate (MgSA), while the carbon chain of SA would strongly interlock with PTMC because of their similar polarity.[32–34] Moreover, the SA layer could fill the gap between $Mg(OH)_2$ and PTMC, preventing the corrosive medium permeation and subsequent pitting corrosion.

Last but not the least, to advance the clinical applications, the chosen components of the composite coating are not only biocompatible, biodegradable, inexpensive, and large-scale producible, but also of translational potential. The $Mg(OH)_2$ layer is biodegradable, which would degrade into Mg^{2+} and OH^- gradually.[35] SA is a natural fatty acid,[36] and PTMC is also biodegradable.[37] Moreover, SA and PTMC have been approved by U.S. Food and Drug Administration, demonstrating their translational promise.[38,39]

2.2. Fabrication and Characterization of AZ31-OH&SA@PTMC

The AZ31-OH&SA@PTMC was fabricated by using the approach shown in Figure 1. The fabrication process was first followed by scanning electron microscopy (SEM) imaging. As shown in **Figure 2**a, the AZ31 had a relatively smooth surface. After the hydrothermal treatment, the obtained AZ31-OH had compact sheet-like micro-nano structures. The micro-nano structures were retained after further coating of SA on AZ31-OH. Interestingly, after PTMC coating, the obtained AZ31-OH&SA@PTMC exhibited smoother surface morphologies than the other three samples. Furthermore, the morphologies of the samples were also different from electrodeposited surfaces, cold sprayed surfaces, burnished surfaces, and so on.[20,22,23] It indicated that the surface morphology was determined by coating materials and technology.

To further reveal the structure of AZ31-OH&SA@PTMC, the cross-sectional morphology imaging and energy dispersive spectroscopy (EDS) elemental mappings were performed. As shown in Figure 2b, the thickness of inner $Mg(OH)_2$ layer and outer PTMC layer was 12.5 ± 0.7 and 10.6 ± 1.2 µm, respectively, which agreed well with the EDS elemental mapping results. Notably, no gap between $Mg(OH)_2$ and PTMC was observed. In contrast, for AZ31-OH@PTMC, a clear gap was

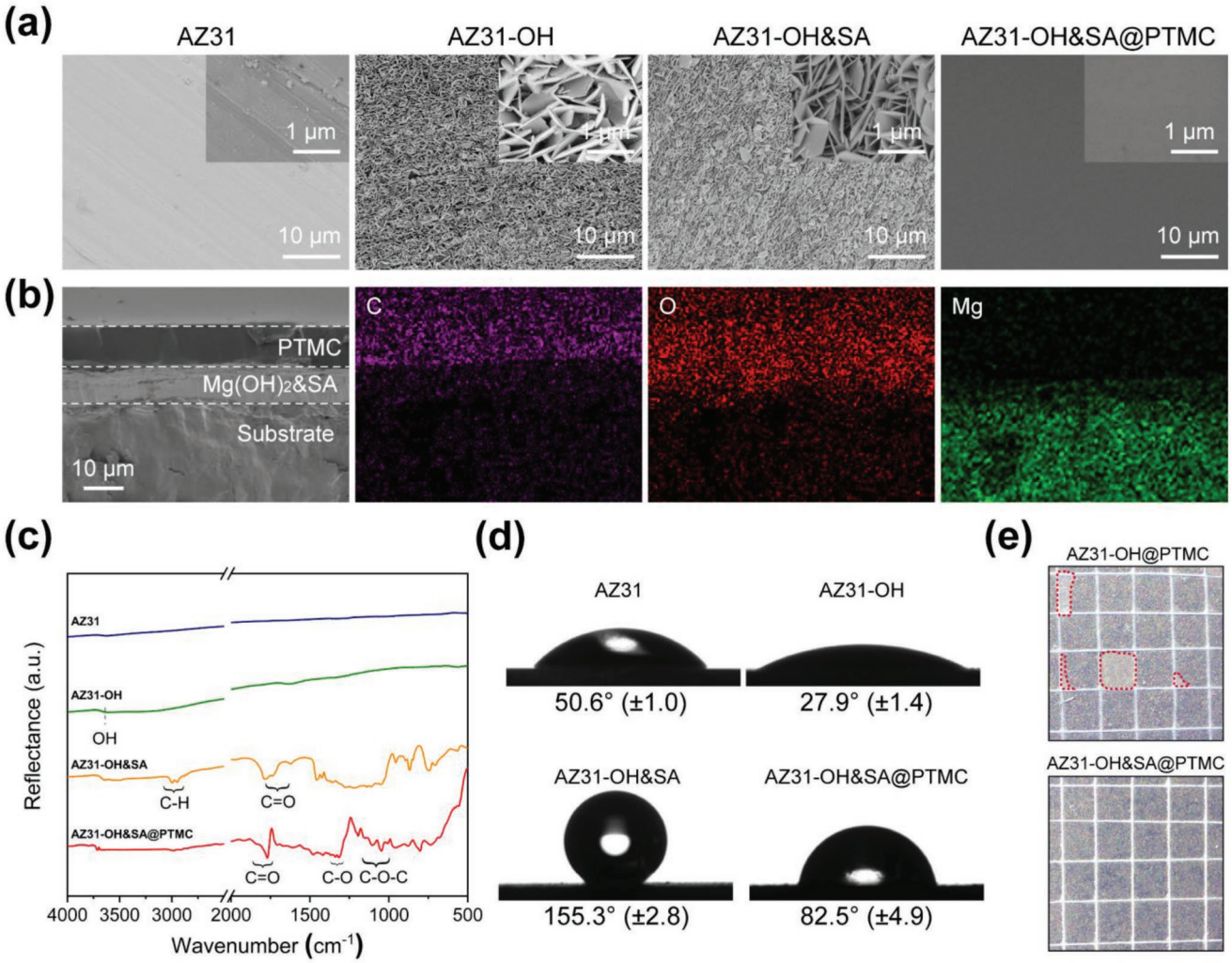

Figure 2. Characterizations of AZ31, AZ31-OH, AZ31-OH&SA, and AZ31-OH&SA@PTMC. a) SEM images of each sample. Inset: magnified SEM images. b) Cross-sectional morphology and EDS elemental mappings (C, O, and Mg) of AZ31-OH&SA@PTMC. c) FTIR spectra and d) water contact angles of each sample. e) Optical images of AZ31-OH@PTMC and AZ31-OH&SA@PTMC after adhesion test (red shapes indicate PTMC removal).

formed between $Mg(OH)_2$ and PTMC, which was also confirmed by the EDS elemental mapping results (Figure S1, Supporting Information). These results demonstrated the critical role of SA in forming the compact structure of AZ31-OH&SA@PTMC.

The fabrication process was also followed by Fourier transform infrared spectroscopy (FTIR), X-ray diffraction (XRD), X-ray photoelectron spectroscopy (XPS), and water contact angles measurements. As the FTIR spectra shown in Figure 2c, AZ31 did not show any features. A weak peak attributed to OH was observed for AZ31-OH, agreeing with the formation of $Mg(OH)_2$. New peaks of the C—H asymmetric bands at 2919 to 3024 cm^{-1}, C=O stretch between 1641 to 1720 cm^{-1}, C—O—C stretch around 1085 cm^{-1}, and ν(C—O) around 1250 cm^{-1} were observed for AZ31-OH&SA and AZ31-OH&SA@PTMC,[34,40] proving the successful incorporation of SA and PTMC. XRD was used to probe the formation of $Mg(OH)_2$ after hydrothermal treatment. As shown in Figure S2 (Supporting Information), obvious diffraction peaks at 33.0°, 38.3°, and 58.8° were observed for AZ31-OH, AZ31-OH&SA, and AZ31-OH&SA@PTMC, which were assigned to the crystalline phases of (100), (101), and (110) of $Mg(OH)_2$, respectively.[31] Note, the characteristic peaks of metallic Mg were observed for all the four samples. The XPS results in Figure S3 (Supporting Information) further confirmed the successful sequential coating of $Mg(OH)_2$, SA, and PTMC onto AZ31. The hydrophilicity of the four samples was investigated by water contact angle measurement. As shown in Figure 2d, the hydrothermal pretreatment of AZ31 increased the hydrophilicity (27.9 ± 1.4°), while the subsequent SA coating increased the hydrophobicity (155.3 ± 2.8°). After the PTMC coating, the surface was converted to hydrophilic again (82.5 ± 4.9°). The water contact angle measurement also demonstrated the successful fabrication of AZ31-OH&SA@PTMC.

To further demonstrate the critical role of SA, the cross-cut tape adhesion test was performed. As shown in Figure 2e, some parts of PTMC were removed from AZ31-OH@PTMC after the adhesion test, while no detachment was found on AZ31-OH&SA@PTMC. These results were consistent with the cross-section imaging results and indicated that the adhesion strength at the interfaces was significantly enhanced with a SA layer.

2.3. In Vitro Degradation

To evaluate the degradation behaviors of the four samples, the production of H_2, Mg^{2+}, and OH^- (i.e., pH) was monitored. Among the four samples, AZ31-OH&SA@PTMC released the least volume of H_2 with the lowest rate (**Figure 3**a, and Figure S4, Supporting Information), the least concentration of Mg^{2+} (0.8 ± 0.5 mg L^{-1} cm^{-2}), and led to the lowest pH value (7.7 ± 0.1) (Figure 3b,c). To further investigate the degradation behaviors, the surface morphologies and chemical compositions of the four samples after 30 d immersion test were observed by optical microscope photographs (OMP), SEM, EDS, and micro-CT. AZ31 was corroded worst and covered with the prism-like crystal products (Figure 3e). The products were predominantly made of magnesium phosphate (Figure S5, Supporting Information). The corroded surfaces and magnesium phosphate products were also observed for AZ31-OH and AZ31-OH&SA. In contrast, the surface of AZ31-OH&SA@PTMC remained smooth and intact with negligible signs of microcracks or micropores, or the formation of magnesium phosphate. The above results demonstrated the best in vitro corrosion resistance behavior of AZ31-OH&SA@PTMC among the four samples. Moreover, AZ31-OH&SA@PLGA swelled up and was ruptured (Figure S6, Supporting Information). This comparison demonstrated the advantages of surface-erosion PTMC over bulk-erosion PLGA in terms of better long-time anticorrosion capability. Furthermore, micro-CT analysis was performed to evaluate the volume change of the samples after immersion test. As the visualized micro-CT 3D models shown in Figure 3e, intact and smooth surface was kept by AZ31-OH&SA@PTMC when compared with the others (especially the surface of AZ31 with obvious corrosion pits). Figure 3d showed the volume loss of AZ31-OH&SA@PTMC was the lowest, about 10.0%, 19.5%, and 21.6% of that of AZ31, AZ31-OH, and AZ31-OH&SA, respectively. These findings confirmed that AZ31-OH&SA@PTMC exhibited excellent corrosion resistance in corrosive medium for 30 d.

To further understand the remarkable corrosion resistance of AZ31-OH&SA@PTMC, electrochemical tests were conducted. The open circuit potential (OCP) curves of the four samples were ranked in a decreasing order as follows: AZ31-OH&SA@PTMC>AZ31-OH&SA≈AZ31-OH>AZ31 (Figure S7a, Supporting Information), which implied that AZ31-OH&SA@PTMC possessed the highest thermodynamic stability than the others. The free corrosion potential E_{corr} and corrosion density j_{corr} were determined by Tafel slope extrapolation as shown in Figure S7 and Table S1 (Supporting Information). Compared with AZ31, the E_{corr} of AZ31-OH&SA@PTMC increased from −1.66 to −1.46 V (vs SCE), decreasing the thermodynamic tendency to electrochemical corrosion. Moreover, the j_{corr} of AZ31-OH&SA@PTMC was 5.05×10^{-10} A^0 cm^{-2}, which was one order, two orders, and six orders of magnitude lower than that of AZ31-OH&SA (3.83×10^{-9} A^0 cm^{-2}), AZ31-OH (1.78×10^{-8} A^0 cm^{-2}), and AZ31 (1.33×10^{-4} A^0 cm^{-2}), respectively.

An anticorrosion mechanism of AZ31-OH&SA@PTMC was proposed. As shown in Figure S8 (Supporting Information), all the components of the sandwiched coating (i.e., $Mg(OH)_2$, SA, and PTMC) synergistically determined the biodegradation behavior of the Mg alloy substrate. The micro-nano structured $Mg(OH)_2$ layer provided an expanded surface area to interface with SA. SA further interlocked with PTMC via hydrophobic interaction to alleviate the incompatibility between $Mg(OH)_2$ and PTMC. The critical role of SA was further revealed by comparing with AZ31-OH@PTMC without an SA layer. The polar $Mg(OH)_2$ interface hindered a perfect filling of nonpolar PTMC, leaving gaps between AZ31-OH and PTMC. Once gaps occurred, they would reduce the adhesion between the two layers. Even worse, the gaps led to porous interface and increased the risks of being penetrated with corrosive medium, which in turn expanded the corrosion area. For AZ31-OH&SA@PTMC, with the assistance of SA, PTMC was able to fill micro-nano structured $Mg(OH)_2$ thoroughly, eliminating gaps and porosity of interfaces, as well as blocking corrosive medium by the hydrophobic SA layer. The outer PTMC layer benefitted the anticorrosion behavior of the coating because of its surface-erosion degradation mode.[26] Unlike bulk-erosion of PLA, PLGA, or

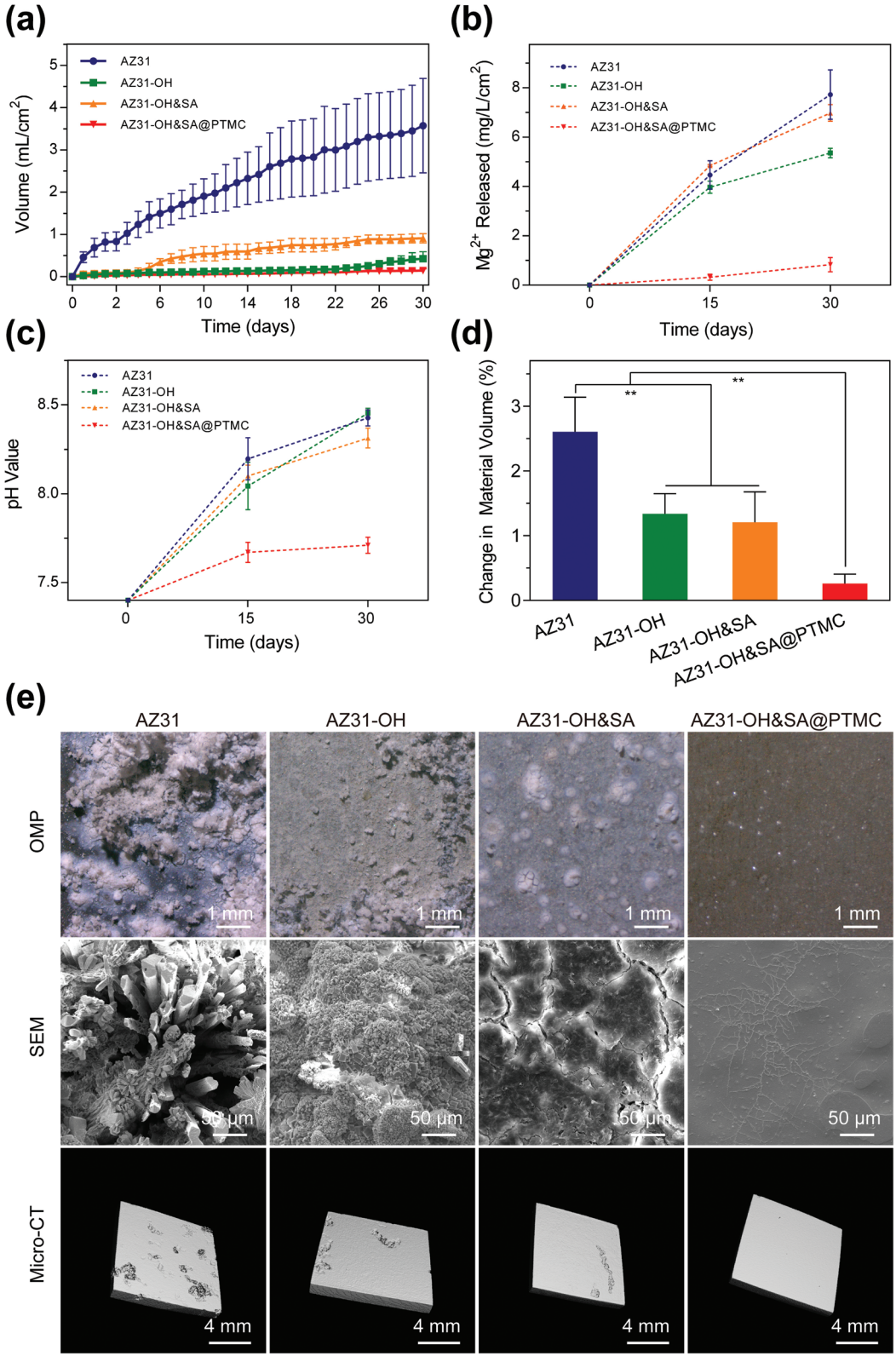

Figure 3. Degradation behaviors of AZ31, AZ31-OH, AZ31-OH&SA, and AZ31-OH&SA@PTMC in vitro. a) Released H_2 volume, b) Mg^{2+} concentration, c) pH value, and d) the change in volume of the four samples for immersion degradation in PBS solution at 37 ± 0.5 °C up to 30 d; $^{**}p < 0.01$. e) OMP (upper), SEM (middle), and micro-CT (lower) images of the four samples after 30 d immersion.

PCL, PTMC followed surface hydrolysable bond cleavage dominated degradation.[41] This led to a linear mass loss and thus a smooth and compact coating with clear degradation boundaries during degradation.[29] Therefore, such a composite coating effectively prevented Mg alloy implants from fast degradation and maintained their integrity and mechanical properties.

2.4. Cytocompatibility Evaluation

It is crucial to enhance cell adhesion, proliferation, and survival on implants for successful bone defect repair. Therefore, we evaluated cell growth, adhesion, and proliferation on AZ31, AZ31-OH, AZ31-OH&SA, and AZ31-OH&SA@PTMC surfaces. The cytoskeletons of cells were stained with FITC-phalloidin (green) (**Figure 4**a). Very few rBMSCs were detected on AZ31, while multibranched rBMSCs were adhered on AZ31-OH and AZ31-OH&SA. Moreover, the most spread rBMSCs were observed on the surface of AZ31-OH&SA@PTMC (Figure 4a). These results indicated the improved cellular adhesion properties of AZ31 after coating (especially the composite coating). The cell coverage area was then analyzed. For both 1 and 3 d after culture, AZ31-OH&SA@PTMC had the highest cell coverage area, while AZ31 had the lowest (Figure 4b). In addition, rBMSCs cultured in the extracts of AZ31-OH, AZ31-OH&SA, and AZ31-OH&SA@PTMC showed greater proliferation ability compared to those in the extract of AZ31 (Figure 4e), due to lower Mg^{2+} concentration released and lower pH value (Figure 4c,d). Similarly, Annexin V/PI staining indicated that the extracts of AZ31-OH, AZ31-OH&SA, and AZ31-OH&SA@PTMC did not cause significant cytotoxicity, while the extract of AZ31 caused higher rBMSCs

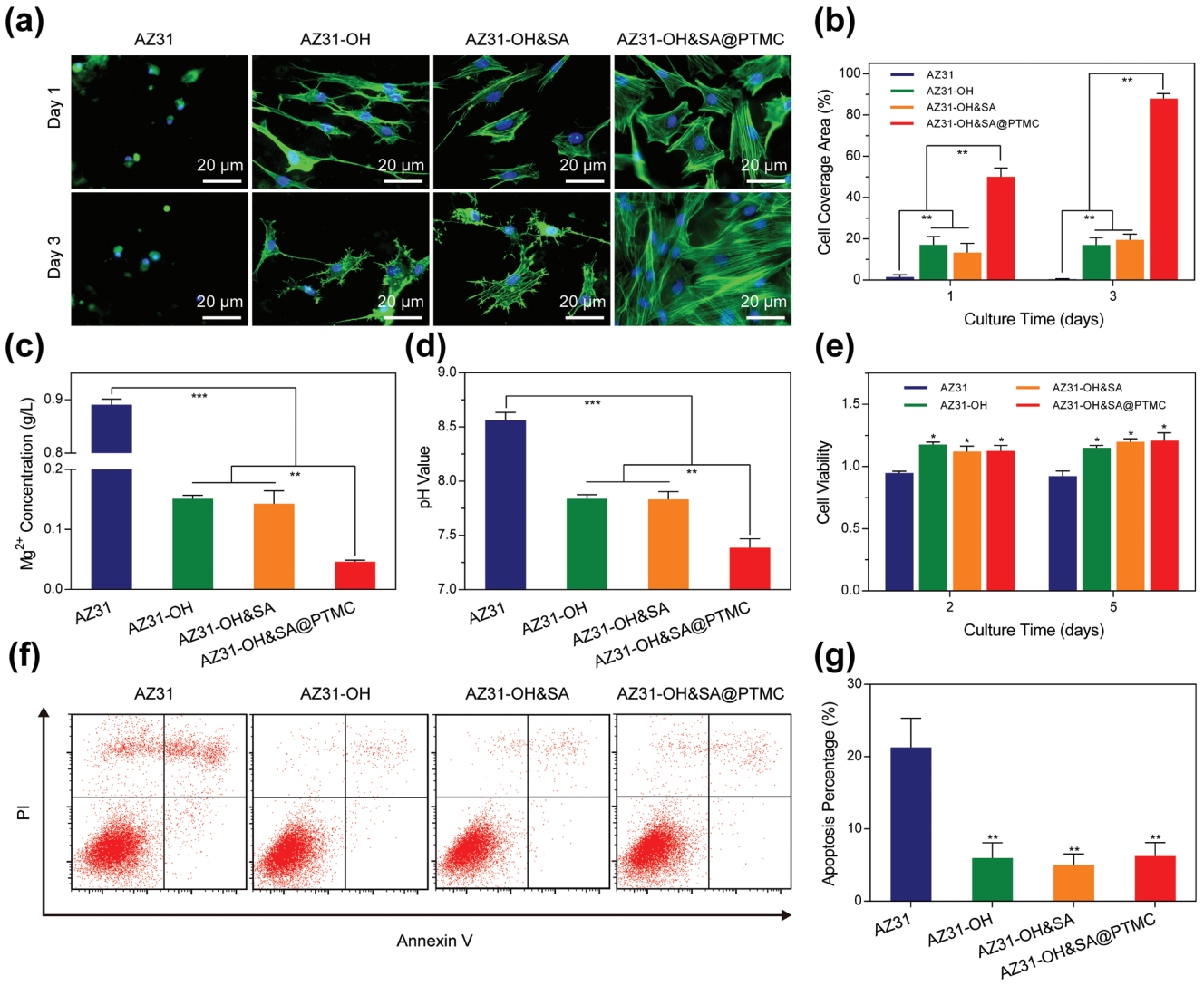

Figure 4. Adhesion and viability of rBMSCs on AZ31, AZ31-OH, AZ31-OH&SA, and AZ31-OH&SA@PTMC surfaces and extracts. a) Fluorescent images of cells cultured on sample surfaces by staining with DAPI (blue) and FITC-phalloidin (green), and b) surface area covered by cells for 1 and 3 d; $^{**}p < 0.01$. c) Mg^{2+} concentration and d) pH value of AZ31, AZ31-OH, AZ31-OH&SA, and AZ31-OH&SA@PTMC extracts in cell culture medium after 24 h incubation; $^{**}p < 0.01$, $^{***}p < 0.001$. e) Viability of rBMSCs incubated in extracts after 2 and 5 d; $^{*}p < 0.05$. f) Apoptosis assays for flow cytometry and g) apoptosis ratio of rBMSCs cultured in extracts for 2 d; $^{**}p < 0.01$.

death and apoptosis (Figure 4f,g). These results suggested that AZ31-OH&SA@PTMC possessed better cytocompatibility than the other three, which could be attributed to the good biocompatibility of AZ31 as well as the coating materials, the proper releasing Mg^{2+} and H_2 concentrations, and the minimized pH variations. The excellent cytocompatibility would enable AZ31-OH&SA@PTMC implants for bone healing in vivo.

2.5. Enhanced Performance of AZ31-OH&SA@PTMC In Vivo

The rods of AZ31, AZ31-OH, AZ31-OH&SA, and AZ31-OH&SA@PTMC were fabricated and implanted into rat femur cavity to evaluate their biocompatibility, anticorrosion property, and bone regeneration ability in vivo. There was no histological abnormality of muscle, liver, kidney, and lung in the four groups after 12-week surgery, suggesting AZ31 and its coatings possessed good histocompatibility in vivo (Figure S9, Supporting Information).

To confirm the correct implant position and to monitor the implant degradation status as well as surrounding tissue healing, micro-CT was performed immediately as well as after 4- and 12-week implantation. Obvious corrosion occurred on PTMC deficient groups (AZ31, AZ31-OH, and AZ31-OH&SA) after 4 and 12 weeks (**Figure 5**a,b). Compared with AZ31, the degree of corrosion on surface of AZ31-OH and AZ31-OH&SA was slightly milder, while AZ31-OH&SA@PTMC possessed the most excellent anticorrosion performance with intact morphologies of the four materials (Figure 5a,b). The quantitative analysis in Figure 5d revealed that the volume loss of AZ31-OH&SA@PTMC was about 28.8% and 14.8% of that of AZ31 at week 4 and week 12, respectively. It's worthy noted that though the anti-corrosion properties of AZ31-OH and AZ31-OH&SA were better than AZ31, the accelerated corrosion was observed for both of them at week 12. These results demonstrated that only AZ31-OH&SA@PTMC has achieved a long-lasting anticorrosion effect.

Apart from the outstanding anticorrosion performance of AZ31-OH&SA@PTMC, it also presented a promising bone regeneration ability. Newly formed bone was observed around AZ31-OH, AZ31-OH&SA, and AZ31-OH&SA@PTMC, and some parts of bare AZ31 (Figure 5b). Furthermore, 3D images and qualitative analysis on new bone formation around midpart of the implants showed about 1.7-fold enhancement of AZ31-OH&SA@PTMC (0.29 ± 0.07 mm^3) compared with AZ31 (0.17 ± 0.04 mm^3) (Figure 5c,e). All above implied AZ31-OH&SA@PTMC could not only protect implants from fast degradation but also enhance bone formation in vivo.

Through the construction of this sandwiched composite coating on Mg alloy implants, the PTMC polymer, as a long-term stable, and highly biocompatible outer layer, stimulated cells adhesion and proliferation as compared with the others (Figure 4a). Interestingly, as the implantation time prolongs, the thinning of PTMC coating could increase the penetration of body fluids and released Mg^{2+} and OH^-. Appropriate concentration of these degradation products could greatly accelerate the new bone formation.[13,16] More importantly, the gradually accelerated, uniform degradation coating could also avoid the too fast local corrosion in the early and middle stages, which was beneficial to the maintenance of implants' mechanical properties.

3. Conclusions

From the perspective of anticorrosion mechanism and clinical applications, a sandwiched coating consisting of biocompatible $Mg(OH)_2$, SA, and PTMC was designed to enhance Mg alloys (e.g., AZ31 herein) implants. Due to the synergistic effects brought by this sandwiched composite coating, biodegradable Mg alloy implant with both mechanical integrity, and regeneration promotion was developed. Only 10.0% and 14.8% corroded volume was observed in AZ31-OH&SA@PTMC implant compared with bare AZ31 in vitro and in vivo, respectively. Furthermore, there was a 1.7-fold enhancement in bone regeneration around AZ31-OH&SA@PTMC compared with bare AZ31. Strategies applied in this design were highlighted: first, a surface-erosion mode of PTMC layers was creatively utilized to reduce fast local corrosion; second, the buffering effect of SA provided an effective approach to reduce the gap at interfaces between inner and outer layers; and third, all components are highly biocompatible for future translational applications. In summary, this study paves a promising way for the development of fully biodegradable and biocompatible orthopedic Mg alloy implants as well as other biomedical products for more safe and efficient tissue engineering.

4. Experimental Section

Preparation Process of Coatings: Raw Mg alloy AZ31 plate (Alfa Aesar, USA) was cut into 10.0 mm × 10.0 mm × 1.0 mm plates for in vitro investigation, and 10.0 mm × 1.0 mm × 1.0 mm rods for in vivo implantation. Then they were polished with SiC abrasive paper progressively up to 7000 grits, ultrasonically cleaned with acetone and ethanol, and dried in air.

There were three steps to prepare AZ31-OH&SA@PTMC. First, $Mg(OH)_2$ layer was grown on AZ31 to obtain AZ31-OH by a hydrothermal method. Typically, the cut small plates (or rods) were placed in a Teflon vessel with a 100 mL capacity filled with 30 mL ultrapure water. The reaction was kept in a Teflon-lined stainless at 160 °C for 3 h.[42] Then samples were rinsed with ethanol and dried in the air. Second, AZ31-OH&SA was prepared by immersing AZ31-OH in 15 mg mL^{-1} of SA (Aladdin, China) ethanol solution at 25 °C for 12 h. Then the samples were washed with ethanol and dried in a vacuum oven. Finally, AZ31-OH&SA@PTMC was fabricated by controlled evaporation of 1 wt% PTMC (M_w, 500 000 *Da*; Jinan Daigang Biomaterial Co., Ltd, China) in dichloromethane onto AZ31-OH&SA with a volatilization rate of 2 mL h^{-1} at 25 °C.[26] For AZ31 rods, a dip-coating method was used.

Characterization of Coatings: OMP of all samples were recorded under an optical microscope (Axio Imager A2m, Zeiss, Germany). Cross-section morphologies and coating thickness of the samples were observed under a field emission scanning electron microscopy (FE-SEM; Ultra 55, Zeiss, Germany). EDS was used to analyze all the samples' elemental compositions. The crystalline phases of the samples were identified by using XRD (ARL-XTRA, Thermo Fisher Scientific, USA) with 2° min^{-1} using a chromium anode. The surface chemical composition of the samples was measured by using XPS (PHI-5000C ESCA, PerkinElmer, USA). The chemical bonds of samples were detected via FTIR (Nexus 870, Nicolet Corp., USA).

Water-contact angle (CA) measurements were performed with a contact angle meter (CA100C, Innuo Co., Ltd, China) based on a sessile drop measuring method with a water droplet volume of 5 µL. Briefly,

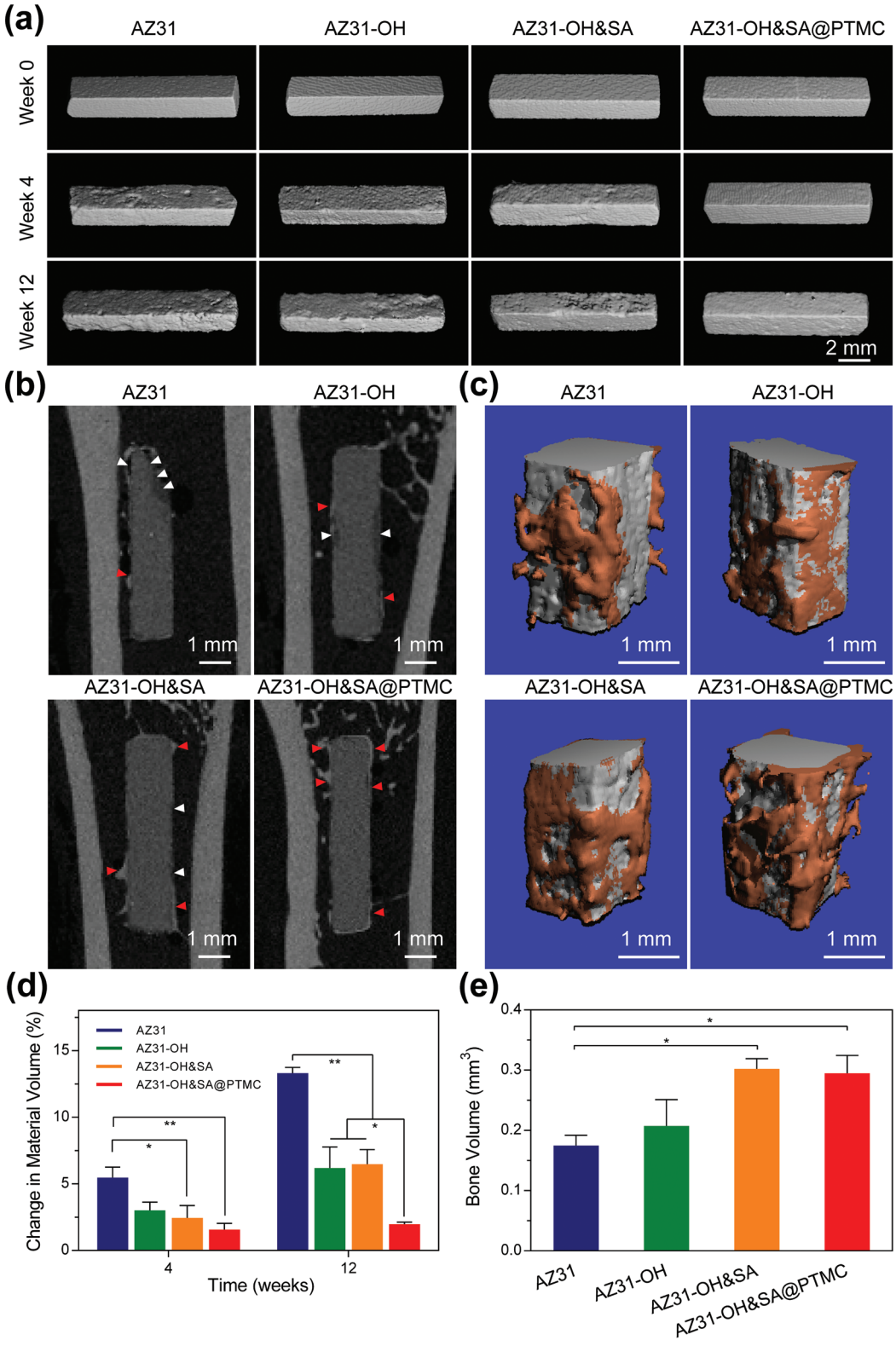

Figure 5. Radiological measurements of implants corrosion and new bone formation in vivo. a) 3D images of different rods before (0 week) and after 4- and 12-week implantation. b) Vertical section images of rods implanted into rat femur cavity after 12-week implantation (white arrows indicate corrosive region and red arrows indicate new bone formation). c) 3D reconstruction models of newly formed bone (orange in color) on implants (white in color) after 12-week implantation. d) The changes of volume of rods after 4- and 12-week implantation and e) new bone formation volume after 12-week implantation; $*p < 0.05$, $**p < 0.01$.

when a droplet of deionized water was applied onto a flat sample surface, the contact angle of the droplet with the surface was measured. Adhesion of the coating on AZ31 was measured according to ASTM D 3359-09.[43] A cutting tool was used to space the cuts 1 mm apart and to make seven cuts. A tape (3M-610, USA) was applied to the freshly cut surface. The tape was rubbed firmly with an eraser on the end of a pencil to ensure good contact with the cut surface. Within 90 ± 3 s of application, the tape was removed rapidly at an angle of near 180°.

Electrochemical Corrosion Tests: The OCP and potentiodynamic polarization (PDP) were obtained by using an electrochemical workstation (CHI660E, ChenHua, China) in PBS at room temperature. PDP test was performed from −2.0 to −1.0 V (vs saturated calomel electrode, SCE) at a scanning rate of 1 mV s^{-1}. The corrosion potential E_{corr} and current density j_{corr} were determined by the Tafel method through linear extrapolation of active polarization zone (in cathodic polarization section when the over potential was about 50 mV less than free corrosion potential).

In Vitro Immersion Tests: Immersion test in corrosive solution was conducted to evaluate the long-term corrosion resistance of the samples. Briefly, every four samples were encapsulated in an epoxy resin block with a test area of 4 × 1 cm^2. The hydrogen gas was collected by using an eudiometer fixed up-side-down capping over the tested sample immersed in 400 mL PBS. Meanwhile, the pH value was measured by using a STARTER 3100 pH meter (OHAUS, USA) and the Mg^{2+} concentration was measured by using inductively coupled plasma mass spectrometry (ICP-MS; Optima 5300DV, Perkin Elmer, USA). The number of tests for each sample was no fewer than three for statistical analysis. The rate of hydrogen evolution can be calculated using the following equations

$$r = V/st \tag{1}$$

where r (mL cm^{-2} d^{-1}) is the rate of hydrogen evolution, V (mL) is the volume of hydrogen evolution, s (cm^2) is the surface area, and t (day) is the immersion time, respectively.

Surface morphology and products of the samples after immersion test were observed by using OMP, SEM, EDS, and XRD, respectively. Before and after the immersion test, micro-CT scanning (vivaCT 80, Scanco Medical AG, Switzerland) was used to evaluate the volume loss of the samples. The parameters for X-ray tube were set at as 70 kV (tube voltage), 114 mA (tube current), and 15.6 µm (an isotropic voxel size). The resulting gray-images were segmented using a fixed threshold and low-pass filter to minimize the noise (Sigma = 0.8, support = 1.0, and threshold = 184).

Cell Morphology and Proliferation: Rat bone mesenchymal stem cells (rBMSCs; Cyagen, China) were cultured under 37 °C, 5% CO_2, and 95% relative humidity in standard growth medium consisting of DMEM/F12 (Gibco, USA) containing 10% fetal bovine serum (Gibco, USA) and 1% penicillin and streptomycin (P/S; Gibco, USA). rBMSCs were seeded on the sample surface with a density of 5 × 10^4 cell mL^{-1} in 24-well plates. The morphologies of actin cytoskeleton of cells were investigated at day 1 and day 3. Briefly, cells were washed with PBS, fixed with 4% paraformaldehyde (Sangon, China), permeabilized with 0.1% Triton (Sigma, USA) and blocked in 1 wt% bovine serum protein (CST, USA). F-actins were stained with FITC phalloidin (Cytoskeleton, USA) at 37 °C in the dark for 1 h. Nuclei were stained with DAPI (SouthernBiotec, USA). All the cells were observed by using a fluorescence microscope (Axio Observer A1, Zeiss, Germany).

Cell Apoptosis and Viability: After sterilized by ultraviolet irradiation, AZ31, AZ31-OH, AZ31-OH&SA, and AZ31-OH&SA@PTMC samples were placed in DMEM/F12 medium at a sample surface area-to extraction medium volume ratio of 0.25 cm^2 mL^{-1}. After 24 h incubation, the extracts of the four samples were collected. The Mg^{2+} concentration was analyzed by using ICP-MS and the pH value was measured by using a STARTER 3100 pH meter. rBMSCs with a density of 1 × 10^4 cell mL^{-1} were cultured in 6-well culture plates for 1 d. Then the culture medium was replaced with the extracts for another 2 d. The apoptotic effect of the extracts was examined by using an Annexin V Apoptosis Detection Kit (BD, USA). To test the cell viability, 200 µL of cell suspensions was added to each well of 96-well culture plates. After 24 h, the culture medium was replaced with 100 µL of extracts and the cells were incubated for another 3 and 5 d. Culture medium without the extracts served as the control group. At each time point, the cells were washed with PBS and added Cell Counting Kit-8 (CCK-8; Bimake, China) in each well. After 1 h of incubation, the optical density at 450 nm was measured by using a microplate reader (Multiskan GO, Thermo Fisher Scientific, USA).

The viability of cells was calculated using the equation

$$\text{viability} = \frac{O_t}{O_c} \times 100\% \tag{2}$$

where O_t is the absorbance of the testing samples and O_c is the absorbance of the control groups.

Femur Defect Model in Rats: The anesthetic, surgical, and postoperative care protocols were examined and approved by the Animal Ethics Committee of Nanjing Drum Tower Hospital and conducted under the Institutional Committee of Care and Use of Laboratory Animals. Two-month-old male Sprague–Dawley rats weighing ≈200 g from the Experimental Animal Center of Nanjing Medical University were used in this study. The animals were randomized into four groups (six animals each group) with implantation time point of 4 or 12 weeks. Two femurs of each rat underwent the same surgical procedure by intramedullary implanting Mg alloy rods. Under anesthesia induced by subcutaneous administration of 30 mg mL^{-1} pentobarbital sodium, a medial patella arthrotomy was performed to expose the knee joint. A hole (φ = 1.0 mm) was drilled through intercondylar fossa so that the Mg alloy rods could be implanted longitudinally into the medullary cavity. AZ31, AZ31-OH, AZ31-OH&SA, and AZ31-OH&SA@PTMC rods with size 1.0 mm × 1.0 mm × 10.0 mm were implanted, respectively.

Radiology: Rats were sacrificed at 4- and 12-weeks postsurgery, and the femurs with implants were harvested. To assess the progress of bone healing and implant degradation, micro-CT scanning was performed. X ray-tube set at 70 kV, 114 mA at a resolution of 17.5 µm with an integration time of 250 ms. The volume of implants and new bone formed around implants was measured via 3D reconstruction of series of 2D tomography images. The region of interest was selected from 2D images with a standardized threshold (>184) as implants and with a threshold (>220) as mineralized bone.

Histological Analysis: In addition to femur samples, quadriceps femoris muscle, liver, lung, and kidney were collected. These soft tissues were fixed in 4% polyformaldehyde (Biosharp, China), dehydrated in graded alcohol solutions, and then embedded in paraffin. Histological sections (≈5 µm) were stained with hematoxylin and eosin, and imaged by using a bright-field microscope (DM 1000, Leica, Germany).

Statistical Analysis: The statistical significance of differences between groups was determined by using one-way ANOVA followed by Tukey post-hoc analysis. Significance was established by a value of $p < 0.05$. Statistical analysis was performed with GraphPad Prism 6.

Supporting Information

Supporting Information is available from the Wiley Online Library or from the author.

Acknowledgements

Y.L. and S.Z. contributed equally to this work. This work was supported by the Projects of International Cooperation and Exchanges NSFC (No. 81420108021), NSFC (Nos. 81772402, and 81802152), Jiangsu Provincial Key Medical Center Foundation, Jiangsu Provincial Medical Talent Foundation, Jiangsu Provincial Medical Outstanding Talent Foundation, Jiangsu Science and Technology Project (Youth Fund BK20160633), Open Funds of the State Key Laboratory of Analytical

Chemistry for Life Science (SKLACLS1704), Open Funds of the State Key Laboratory of Coordination Chemistry (SKLCC1819), Fundamental Research Funds for the Central Universities (021314380145), and the Scientific Research Foundation of Graduate School of Nanjing University (2016CL12).

Conflict of Interest

H.W., Q.J., Y.Z., M.S., Y.L., S.Z., and D.Z. are the authors of the related patents.

Keywords

biodegradable implants, bone generation, composite coatings, magnesium alloy

Received: August 12, 2019
Revised: October 25, 2019
Published online: November 22, 2019

[1] M. Geetha, A. K. Singh, R. Asokamani, A. K. Gogia, *Prog. Mater. Sci.* **2009**, *54*, 397.
[2] S. Nishiguchi, T. Nakamura, M. Kobayashi, H.-M. Kim, F. Miyaji, T. Kokubo, *Biomaterials* **1999**, *20*, 491.
[3] T. Takizawa, N. Nakayama, H. Haniu, K. Aoki, M. Okamoto, H. Nomura, M. Tanaka, A. Sobajima, K. Yoshida, T. Kamanaka, *Adv. Mater.* **2018**, *30*, 1703608.
[4] J. H. Lonner, M. Klotz, C. L. Levitz, P. A. Lotke, *J. Arthroplasty* **2001**, *16*, 107.
[5] T. Nishino, H. Mishima, H. Kawamura, Y. Shimizu, S. Miyakawa, N. Ochiai, *J. Arthroplasty* **2013**, *28*, 1736.
[6] P. Meagher, E. D. O'Cearbhaill, J. H. Byrne, D. J. Browne, *Adv. Mater.* **2016**, *28*, 5755.
[7] A.-M. Pobloth, S. Checa, H. Razi, A. Petersen, J. C. Weaver, K. Schmidt-Bleek, M. Windolf, A. Á. Tatai, C. P. Roth, K.-D. Schaser, *Sci. Transl. Med.* **2018**, *10*, eaam8828.
[8] B. Zberg, P. J. Uggowitzer, J. F. Loffler, *Nat. Mater.* **2009**, *8*, 887.
[9] Y. Liu, Y. Zheng, X. H. Chen, J. A. Yang, H. Pan, D. Chen, L. Wang, J. Zhang, D. Zhu, S. Wu, *Adv. Funct. Mater.* **2019**, *29*, 1805402.
[10] W. Xu, N. Birbilis, G. Sha, Y. Wang, J. E. Daniels, Y. Xiao, M. Ferry, *Nat. Mater.* **2015**, *14*, 1229.
[11] F. Witte, V. Kaese, H. Haferkamp, E. Switzer, A. Meyerlindenberg, C. J. Wirth, H. Windhagen, *Biomaterials* **2005**, *26*, 3557.
[12] A. Chaya, S. Yoshizawa, K. Verdelis, N. Myers, B. J. Costello, D. T. Chou, S. Pal, S. Maiti, P. N. Kumta, C. Sfeir, *Acta Biomater.* **2015**, *18*, 262.
[13] Y. Zhang, J. Xu, Y. C. Ruan, M. K. Yu, M. Olaughlin, H. Wise, D. Chen, L. Tian, D. Shi, J. Wang, *Nat. Med.* **2016**, *22*, 1160.
[14] F. Witte, *Acta Biomater.* **2010**, *6*, 1680.
[15] J. Park, P. Du, J. K. Jeon, G. H. Jang, M. P. Hwang, H. S. Han, K. Park, K. H. Lee, J. W. Lee, H. Jeon, *Angew. Chem., Int. Ed.* **2015**, *54*, 14753.
[16] Z. Lin, J. Wu, W. Qiao, Y. Zhao, K. Wong, P. K. Chu, L. Bian, S. Wu, Y. Zheng, K. Cheung, *Biomaterials* **2018**, *174*, 1.
[17] H. M. Wong, K. W. Yeung, K. O. Lam, V. Tam, P. K. Chu, K. D. Luk, K. M. Cheung, *Biomaterials* **2010**, *31*, 2084.
[18] B. Li, Y. Han, K. Qi, *ACS Appl. Mater. Interfaces* **2014**, *6*, 18258.
[19] Y. Wang, B. Liu, X. a. Zhao, X. Zhang, Y. Miao, N. Yang, B. Yang, L. Zhang, W. Kuang, J. Li, *Nat. Commun.* **2018**, *9*, 4058.
[20] L. Qin, C. Dexin, K. Zhixin, *ACS Appl. Mater. Interfaces* **2015**, *7*, 1859.
[21] M. Korzynski, T. Zarski, *Surf. Coat. Technol.* **2016**, *307*, 590.
[22] Y. K. Wei, Y. J. Li, Y. Zhang, X. T. Luo, C. J. Li, *Corros. Sci.* **2018**, *138*, 105.
[23] S. Bagherifard, D. J. Hickey, S. Fintová, F. Pastorek, I. Fernandez-Pariente, M. Bandini, T. J. Webster, M. Guagliano, *Acta Biomater.* **2018**, *66*, 93.
[24] L. Li, L. Cui, R. Zeng, S. Li, X. Chen, Y. Zheng, M. B. Kannan, *Acta Biomater.* **2018**, *79*, 23.
[25] Y. Xie, L. Yao, Z. Zhang, A. Lv, X. Shi, *Polym. Compos.* **2016**, *37*, 1369.
[26] J. Wang, Y. He, M. F. Maitz, B. Collins, K. Xiong, L. Guo, Y. Yun, G. Wan, N. Huang, *Acta Biomater.* **2013**, *9*, 8678.
[27] R. Zeng, L. Cui, K. Jiang, R. Liu, B. Zhao, Y. Zheng, *ACS Appl. Mater. Interfaces* **2016**, *8*, 10014.
[28] A. P. Pêgo, A. A. Poot, D. W. Grijpma, J. Feijen, *Macromol. Biosci.* **2002**, *2*, 411.
[29] B. F. Von, L. Schedl, A. Göpferich, *Biomaterials* **2002**, *23*, 4221.
[30] T. Ishizaki, M. Sakamoto, *Langmuir* **2011**, *27*, 2375.
[31] T. Ishizaki, S. Chiba, K. Watanabe, H. Suzuki, *J. Mater. Chem. A* **2013**, *1*, 8968.
[32] W. F. Ng, M. H. Wong, F. T. Cheng, *Surf. Coat. Technol.* **2010**, *204*, 1823.
[33] H. Huang, M. Tian, J. Yang, H. Li, W. Liang, L. Zhang, X. Li, *J. Appl. Polym. Sci.* **2008**, *107*, 3325.
[34] W. Zhang, Y. Chen, M. Chen, S. Zhao, J. Mao, A. Qu, W. Li, Y. Zhao, N. Huang, G. Wan, *Corros. Sci.* **2016**, *112*, 327.
[35] C. Janning, E. Willbold, C. Vogt, J. Nellesen, A. Meyer-Lindenberg, H. Windhagen, F. Thorey, F. Witte, *Acta Biomater.* **2010**, *6*, 1861.
[36] S. Foraita, Y. Liu, G. L. Haller, E. Baráth, C. Zhao, J. A. Lercher, *ChemCatChem* **2017**, *9*, 195.
[37] A. Sorkio, S. Haimi, V. Verdoold, K. Juuti-Uusitalo, D. Grijpma, H. Skottman, *J. Tissue Eng. Regener. Med.* **2017**, *11*, 3134.
[38] J. E. Hunter, J. Zhang, P. M. Kris-Etherton, *Am. J. Clin. Nutr.* **2010**, *91*, 46.
[39] L. Q. Yang, D. Yang, Y. M. Guan, J. X. Li, M. Li, *J. Appl. Polym. Sci.* **2012**, *124*, 3714.
[40] M. Källrot, U. Edlund, A.-C. Albertsson, *Biomaterials* **2006**, *27*, 1788.
[41] J. J. Rongen, B. van Bochove, G. Hannink, D. W. Grijpma, P. Buma, *J. Biomed. Mater. Res., Part A* **2016**, *104*, 2823.
[42] T. Ishizaki, Y. Masuda, M. Sakamoto, *Langmuir* **2011**, *27*, 4780.
[43] ASTM D3350, *Standard Test Methods for Measuring Adhesion by Tape Test*, ASTM International, West Conshohocken, PA **2009**.

